PAPER • **OPEN ACCESS**

Polymer-mixed Sb_2Te_3/Te nanocomposites exhibiting p-type to n-type conduction reversal and thermal conductivity reduction

To cite this article: Dilip Kumar Meena *et al* 2023 *Mater. Res. Express* **10** 074001

Materials Research Express

PAPER

Polymer-mixed Sb_2Te_3/Te nanocomposites exhibiting p-type to n-type conduction reversal and thermal conductivity reduction

Dilip Kumar Meena[1,2,*], **Rapaka S C Bose**[1,5], **A M Umarji**[3] and **D Arvindha Babu**[4]

[1] Department of Physics, Indian Institute of Science, Bengaluru 560012, India
[2] Department of Physics, HNB Garhwal University, Badshahi Thaul Campus, Tehri Garhwal, Srinagar, 249199, India
[3] Materials Research Centre, Indian Institute of Science, Bengaluru 560012, India
[4] Defence Metallurgical Research Laboratory, Hyderabad, India
[5] Presently at the Centre for Materials for Electronics Technology, Thrissur, Kerala, 680581, India.
[*] Author to whom any correspondence should be addressed.

E-mail: dilipmeena@iisc.ac.in

Keywords: thermoelectric, polycrystalline, nanocomposites, thermal conductivity

OPEN ACCESS

RECEIVED
24 February 2023

REVISED
27 May 2023

ACCEPTED FOR PUBLICATION
29 June 2023

PUBLISHED
11 July 2023

Abstract

Sb_2Te_3-based materials are potential room-temperature thermoelectric materials. In the present work, we choose polycrystalline Sb_2Te_3/Te nanocomposites and utilize Poly Methyl Methacrylate (PMMA) to reduce the thermal conductivity of Sb_2Te_3 samples. PMMA and polycrystalline Sb_2Te_3/Te were well mixed using ball milling. Pellets have been made by the cold press method. Thermoelectric transport properties of Sb_2Te_3/Te nanocomposites: composition, microstructure, and analysis are found to be influenced by PMMA. With increasing PMMA concentration a p-type to n-type transition has been observed because there are fewer charge carriers or the composites have a higher resistance. It is also observed that the thermal conductivity of Sb_2Te_3/Te nanocomposites decreases as the PMMA increases. This research paves the way for making the best thermoelectric materials by reducing thermal conductivity through the use of polymers.

1. Introduction

One of the things we frequently encounter and are aware of is energy, which can take several forms. Various forms of energy, including light, sound, electricity, heat, wind energy, etc can be converted into one another directly or indirectly. Electrical energy can be converted into thermal energy with the help of thermoelectrics. Thermoelectric (TE) energy conversion technology has recently attracted a lot of attention because of its advantages over other energy conversion methods. TE materials have a very low impact on the environment and lack moving components [1]. The dimensionless figure of merit, $zT = S^2\sigma T\kappa^{-1}$, which takes the Seebeck coefficient, electrical conductivity, absolute temperature, and thermal conductivity, respectively into account, can be used to describe the performance of TE materials [2]. Polymer-based thermoelectric materials are gaining much attention because of the ability of the polymer in altering the microstructure which can help in tuning the thermoelectric properties [3]. The TE properties of materials, Seebeck coefficient (S), electrical conductivity (σ), and thermal conductivity (κ) are dependent on the quenching medium, i.e., the cooling rate of melt solidification [4–6], annealing treatment [7, 8], the synthesis process [9, 10], and sintering process [11, 12]. Knowledge of the phase diagram is important in choosing the appropriate composition and process temperature. The properties of the TE materials can be tuned by altering the microstructure. By adding a polymer with TE material, the microstructure can be modified which in turn can tune the physical properties of the material [3].

Also, polymer-based TE materials and their composites can be utilized to produce flexible TE material that can be utilized as a wearable thermoelectric generator for energy harvesting and for many other related applications like temperature-controlled body suits [13, 14].

For room-temperature applications, Sb_2Te_3 is one of the best p-type thermoelectric materials [12, 15]. To improve the TE efficiency of Sb_2Te_3 several efforts have been made like the formation of nanocomposite

[16–23], doping [15], orientation engineering [24], and nanostructuring [25, 26]. The formation of nanocomposite has got much attention due to its advantage in reducing thermal conductivity while maintaining a high value of power factor ($PF = S^2\sigma$) [27, 28].

In recent years, polymer-based composites such as poly (3,4-ethylene dioxythiophene) (PEDOT) [3, 4], polyaniline (PANI) [5, 6], and polythiophene [7] have been applied as TE materials due to their versatile processability, low density, and low thermal conductivity, all of which are critical in improving TE properties. Recent research has concentrated on the synthesis of hybrid Sb_2Te_3 composites by the blending of inorganic and organic ingredients to increase their application [29].

In recent years, inorganic-organic composites have attracted much attention as thermoelectric materials due to their versatile advantages such as low thermal conductivity, low density, and easy processability. By using inorganic-organic composites, bilateral benefits of good electrical conductivity with enhanced Seebeck coefficient by decoupling σ and S through an energy filtering effect and with low thermal conductivity can be achieved. Several groups have demonstrated the improved thermoelectric properties of using inorganic material and polymer composites [29–37].

Numerous thermoplastic polymers such as polyethylene (PE), polystyrene (PS), polyvinyl chloride (PVC), polyvinyl acetate (PVA), and polymethyl methacrylate (PMMA) were used as insulating polymer matrix to fabricate composite materials [29, 34–37]. Among them, poly (methyl methacrylate) (PMMA) has been one of the most widely studied polymer materials due to its excellent mechanical, chemical, and thermal stability properties. Conductive pathways can be generated with various inorganic fillers in the interfacial regions of the polymeric matrix during processing [35, 36]. Because the arrangement of inorganic fillers with attractive electrostatic force depends heavily on the matrix shape, the composite could demonstrate high performance with a lined-up conductive pathway.

It is reported that composite formation with polymer (polyvinylpyrrolidone (PVP)) has reduced the κ of Bi_2Te_3-based nanofiber [30]. However, there are not much work on the polymer mixed Sb_2Te_3 nanocomposites.

Among several inorganic materials, the Bi_2Te_3/Sb_2Te_3-based thermoelectric materials were successfully utilized in room-temperature thermoelectric device applications. numerous studies were investigated for n-type Bi_2Te_3 polymer composites and on the other hand few studies only reported for the p-type Sb_2Te_3. In both the n-type and p-type chalcogenides, reducing thermal conductivity and improving the Seebeck coefficient without affecting their electrical conductivity is the main motive to achieve high-performance thermoelectric materials. In the present study, we intend to study the p-type Sb_2Te_3 and PMMA polymer composites due to the benefits of easy processability, large-scale processing of bulk compounds with excellent mechanical, chemical, and thermal stability properties of PMMA towards the improvement of Seebeck coefficient and reduction of thermal conductivity.

Among several inorganic materials, the Bi_2Te_3/Sb_2Te_3-based thermoelectric materials were successfully utilized for in room-temperature thermoelectric device applications. numerous studies were investigated for n-type Bi_2Te_3 polymer composites and on the other hand few studies only reported for the p-type Sb_2Te_3. In both the n-type and p-type chalcogenides, reducing thermal conductivity and improving the Seebeck coefficient without affecting their electrical conductivity is the main motive to achieve high-performance thermoelectric materials.

None of the investigations have been published to investigate the thermoelectric characteristics of PMMA-mixed Sb_2Te_3 nanocomposites. The inorganic material in this study is Sb_2Te_3/Te and the polymer used is PMMA which is a non-conducting polymer. In the conducting pathways of Sb_2Te_3/Te, the polymer will act as an energy barrier that will restrict the transport of electrons as well as scattering centers to restrict the heat flow by scattering the phonons. It is well reflected in the temperature-dependent electrical conductivity and thermal conductivity of Sb_2Te_3 and PMMA polymer composites. The thermal conductivity of Sb_2Te_3 nanocomposites is found to be considerable. The variation in TE properties was understood based on the structural changes due to the addition of polymer.

2. Experiments and methods

Sb_2Te_3/5%Te nanocomposites were synthesized by melting the raw materials, Sb and Te (99.99% purity, Sigma Aldrich) by melt quenching method. Weighing was done on the Sb and Te elemental powders according to the Sb_2Te_3/5%Te composition. The weighed powders were transferred in a quartz ampoule and sealed under a vacuum of 10^{-6} mbar. The ampoule was heated to 1073 K at a rate of 5 K min^{-1} in a rocking resistive furnace. The combination was subjected to a 10-hour rocking motion at 20 rpm and then the ampoule was quenched in an ice water medium. The ingots were ground to powder and then mixed with PMMA powder according to $PMMA_xSb_2Te_3$/5%Te (x = 0.00, 0.01, 0.03, 0.05) ratio. These mixed powders were ball milled for 6 h at 250 rpm in a planetary ball milling system and then cold pressed to produce pellets. The obtained pellets were sintered at

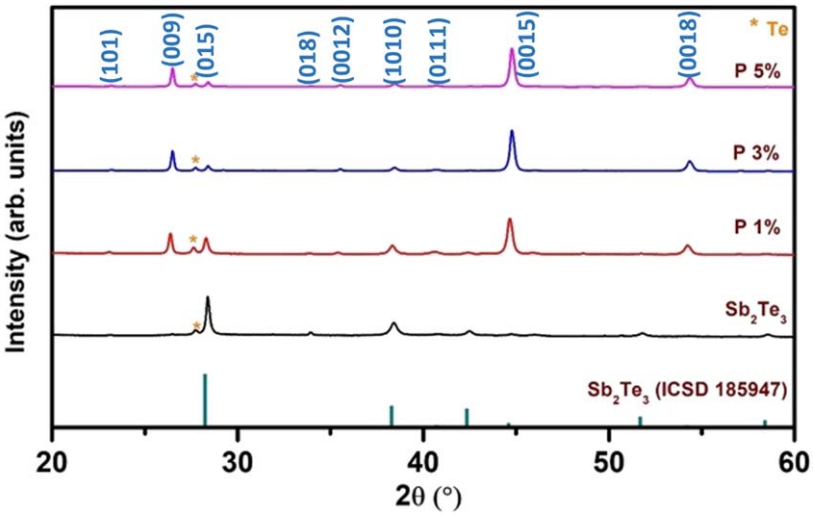

Figure 1. XRD patterns of $PMMA_xSb_2Te_3$/5%Te (x = 0.00, 0.01, 0.03, 0.05) indexed with the rhombohedral phase and marked with secondary phase peaks.

423 K for 6 h under a vacuum of 10^{-3} mbar. This sintering temperature was kept low to avoid any decomposition or melting of the polymer. The density of the sintered pellets was measured using Archimedes' principle. For various structural and thermoelectric studies, the final samples were cut in the desired directions. Under identical conditions, all the samples were made twice and the structural and TE characterizations were independently carried out on these two sets of samples and the average of the two being used.

X-ray diffraction (XRD) was used to determine the crystal structure and purity of the samples using the Rigaku Smart Lab x-ray diffractometer with Cu K_α radiation source ($\lambda = 1.5418$ Å). The sample's Raman spectra were recorded using a HORIBA JOBIN YVON HR 800 confocal Raman spectrometer ($\lambda_{exc} = 532$ nm) and a 12 mW laser. For surface imaging, FEI Quanta 450 scanning electron microscopy (SEM) was used. Backscattered electron (BSE) images were taken with an FEI ESEM-Quanta 200. The powder samples were examined using a JEOL 2000 FX-II transmission electron microscope (TEM). Energy-dispersive x-ray spectroscopy (EDX) was used to determine the elemental compositions. The four probe and bridge methods, respectively, were used to measure the TE transport characteristics, σ and S in the temperature range of 300–390 K using a homemade setup under a vacuum of 10^{-3} mbar. The uncertainty in electrical resistivity (σ) and Seebeck coefficient measurements (S) is ±5%. Hall effect measurement has been done for all the samples at room temperature using a homemade laboratory setup. The heat capacity was calculated using the formula $\kappa = \alpha C_p d$, where α is the thermal diffusivity, d is the density, and Cp is the heat capacity. In the temperature range 300–390 K, the thermal transport properties, thermal diffusivity (α) under argon atmosphere, and heat capacity (C_p) under nitrogen (N_2) atmosphere, were measured using LINSEIS LFA 1000 and differential scanning calorimetry apparatus TA SDT650, respectively. The Uncertainty in thermal conductivity (κ) measurements is ±5%.

3. Results and discussion

3.1. Powder XRD analysis

Figure 1 shows the XRD pattern of polymer mixed Sb_2Te_3/Te nanocomposites. The indexing of all the XRD peaks has been done with *p*-type Sb_2Te_3 (space group: $R3\bar{m}\ h$, rhombohedral, PCD Card No. 1216385) and Te phase (space group: $P3_121$, trigonal, PCD Card No: 382599) [16]. Rietveld refinement analysis was carried out using the Full Proof software. The graphs of the XRD Rietveld refinement are displayed in figures 2(a)–(d). The simulated experimental x-ray diffraction patterns are shown by the dark blue line and observed experimental x-ray diffraction patterns are shown by the orange circles, respectively. The difference between the experimental and simulated curves can be seen by the pink continuous line at the bottom. The Bragg positions are shown by the thin, navy blue vertical lines. Table 1 lists the crystallite size, Lotgering factor, density as well as refined lattice parameters (a, b, c, and V). These values are found to be closely matching with the Sb_2Te_3 lattice parameters that have been reported [16]. As vacancies tend to shorten the lattice parameters, the pure Sb_2Te_3 lattice monotonically decreases with increasing polymer content. Two major phases are present in prepared samples as revealed by the Rietveld refinement. Sb_2Te_3 phase has been found as the main phase and Te has been found as a

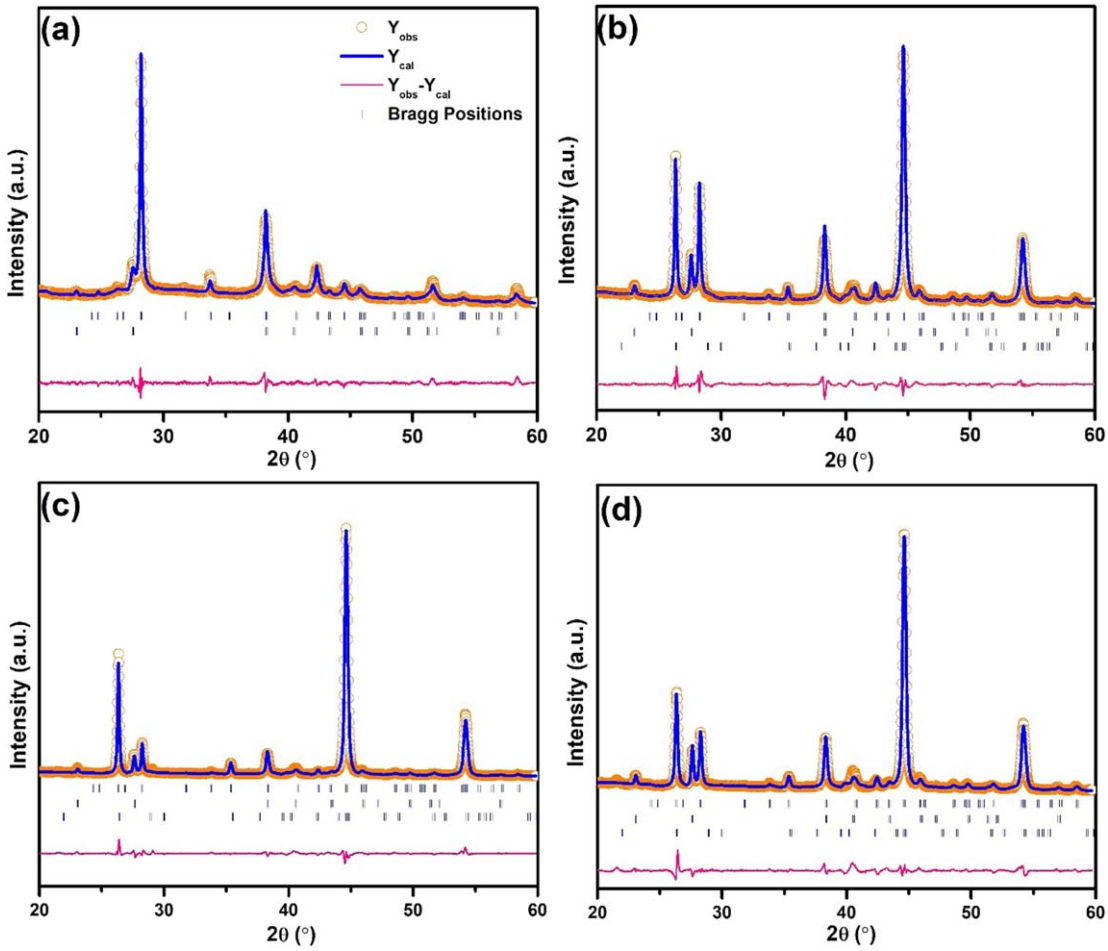

Figure 2. (a)–(d) Rietveld refinement of $PMMA_xSb_2Te_3/5\%Te$ (x = 0.00, 0.01, 0.03, 0.05) samples.

Table 1. Estimated refined lattice parameters, crystallite size, Lotgering factor, density, carrier concentration, and mobility of $PMMA_xSb_2Te_3/5\%Te$ (x = 0.00, 0.01, 0.03, 0.05).

Parameter	Sb_2Te_3	Sb_2Te_3 (1%)	Sb_2Te_3 (3%)	Sb_2Te_3 (5%)
$a = b$ (Å)	4.2701	4.2625	4.2658	4.2593
c (Å)	30.5095	30.4437	30.4467	30.4533
V(Å^3)	481.7686	479.8149	479.0163	478.4668
Lotgering factor	0.0109	0.0281	0.8726	0.7548
Density (g/cm^3)	5.8532 (90%)	5.6235 (86%)	5.4056 (83%)	5.0648 (77%)
Crystallite size (nm)	40.01	36.61	35.96	28.82
Sb_2Te_3 Phase (%)	91.29	83.52	82.20	81.32
Te Phase (%)	8.71	16.46	16.83	18.04
TeO_2Phase (%)	0.00	0.02	0.97	0.64
n_c ($\times 10^{20}$)	1.27	−0.89	−4.83	−25.19
μ	67.21	5.43	0.18	0.065

secondary phase. A trace amount of the secondary phase of Te was observed in all the samples, due to the high amount of nonreactive Te present in the prepared samples.

The Rietveld refinement results show that the increase of polymer content in the Sb_2Te_3/Te composite tends to decrease the Sb_2Te_3 phase and increases the Te phase. This is clearly evident in the observation of the presence of the Te phase (%) which increased from 8% to 18% and a simultaneous decrease in the Sb_2Te_3 phase from 91% to 81% with the increase of polymer content from (0 to 0.05%). These observations show that the addition of polymer may segregate the Te phase from the Sb_2Te_3 phase. In addition to this, the crystallite size, crystallite volume, and density of the polymer composite tend to decrease with the increase of PMMA content. There is a difference in the intensity of the (015) peak and (0015) peak is also observed, suggesting that the polymer mixed samples show a significant anisotropy of grain orientation without changing the crystal structure. The Lotgering

factor (F) is determined to confirm the anisotropic orientation from the XRD patterns of polymer mixed samples.

From XRD peak intensity data, the degree of crystal grain orientation i.e. the Lotgering factor (F) is calculated in the case of layered structure materials since they are arranged mostly along the c-axis. The F is as follows $F = \frac{P - P_0}{1 - P_0}$ Where, $P = \sum I(00l)/\sum I(hkl)$ and $P_0 = \sum I_0(00l)/\sum I_0(hkl)$; Po can be calculated from the peak data of the JCPDS card. The F value is zero ($F = 0$) for a crystallographic isotropic (randomly oriented) sample i.e. the value of P is Po, and the F value is one ($F = 1$) for a completely oriented sample. F is increasing by increasing the polymer quantity which indicates the orientation of planes in a particular direction. Figure 1 shows that after adding the polymer the prepared samples have been oriented on the c-axis. From XRD data, the crystalline sizes (table 1) of the samples are calculated using the Debye–Scherrer's equation $D = \frac{K\lambda}{\beta \cos\theta}$ where D is the crystallite size, K is the shape factor (usually, the value of K is 0.94), λ is the x-ray wavelength (0.15418 nm), and β is the full-width half-maximum (FWHM) of the diffraction peak at θ, which is the diffraction angle. Crystalline size shows a monotonic decrease with increasing polymer content because of the shrinking of the vacancies. Anti-site defects are highly prevalent in the Sb_2Te_3 system, and Sb atoms may occupy Te sites (Sb_{Te}) [38]. This may also be a reason behind the decreasing trend of the volume of prepared samples. Therefore, as described in the section on thermoelectric transport properties, the addition of polymer to the Sb_2Te_3 system may significantly affect the TE properties of Sb_2Te_3/Te nanocomposites.

3.2. Microstructural analysis

Figures 3(a)–(e) displays SEM images of melt-quenched polymer (PMMA) mixed Sb_2Te_3/Te nanocomposites. The grains have a sheet-like shape, as shown in these micrographs. Figures 3(b)–(d) shows the polymer mixed SEM images. The polymer has shown in (b), (c), and (d) images in white color. By increasing the polymer content excess Te has increased because the polymer addition developed inhomogeneity in the nanocomposites. The EDX spectra displayed in figure 3 show the presence of too much Te along with the Sb_2Te_3 matrix. It is obvious that the Te distribution is not constant throughout the polymer mixed samples. Te-Te defects are produced by the secondary Te phase in composite materials, and these defects significantly affect the TE characteristics [39–42]. High-resolution TEM images have been taken to check the phase formation of the Sb_2Te_3 matrix (figure 4(a)). The selected area electron diffraction (SAED) pattern also confirms the phase formation of Sb_2Te_3. The ring pattern indicates the polycrystalline nature of the materials. Distance between the (015) planes has been calculated by ImageJ software and it has matched with the reported data of the Sb_2Te_3 matrix. Figure 4(c) shows the Backscattered-Electron *(BSE)* image of the Sb_2Te_3/Te nanocomposite. Te has shown in dark black colour in figures 4(d)–(f). The addition of polymer increases the nonreactive Te in Sb_2Te_3 which is clearly visible in figures 4(d)–(f). These images reveal that the mixing of polymer (PMMA) has a major impact on the microstructure. Te typically has nanograin sizes in the 30 to 50 nm range. The phonon means free path of Sb_2Te_3 is in the range of nanoscale, which makes the Te nanograins effective in phonon scattering [43]. However, a clear difference has been observed between the pristine and polymer mixed samples. The following discussion discusses how microstructural modifications affect TE characteristics.

3.3. Raman and XPS analysis

To study more about the nanocomposites' molecular mode of vibration, Raman spectroscopy was used. Figures 5(a)–(d) displays the Raman spectra of the polymer mixed Sb_2Te_3/Te composites for x = 0, 0.01, 0.03, and 0.05 that were obtained using a 532 nm laser at room temperature. The silicon standard, which has a Raman peak of 520.5 cm^{-1}, was used to calibrate the Raman spectra. With the use of a Gaussian line profile, Raman peaks were fitted.

Raman scattering is used to identify the three Raman-active phonons ($A_{1g}{}^1$, $E_g{}^2$, and $A_{1g}{}^2$) present in Sb_2Te_3-related compounds. These compounds have a rhombohedral structure made up of hexagonal close-packed atomic layers stacked along the c-axis [26]. The Raman spectra of Sb_2Te_3/Te nanocomposites (figures 5(a)–(d)) clearly display the Raman active vibrational modes at ~65 cm^{-1}, ~87 cm^{-1}, ~116 cm^{-1}, ~137 cm^{-1}, and ~164 cm^{-1} belonging to $A_{1g}{}^1$, E', $E_g{}^2$, A_1, and $A_{1g}{}^2$ respectively [26]. The existence of both Sb_2Te_3 and Te phases is further demonstrated by the fact that three of these vibrational modes $A_{1g}{}^1$, $E_g{}^2$, and $A_{1g}{}^2$ were formed from Sb2Te3, whereas the other two modes E' and A_1 were produced by Te as shown in figure 5(e). This is again an agreement with the XRD results.

Out-of-plane and in-plane vibrations, respectively, are represented by the A_{1g} and E_g modes. Out-of-plane (A_{1g}) vibrations are found to be influenced by the addition of polymer to the Sb_2Te_3/Te composite. Raman peaks of A_{1g} plane vibrations are increasing with increasing polymer content indicating that the samples are oriented along the c-axis. It suggests that the mixing polymer with Sb_2Te_3/Te composite has a major impact on the thermal transfer, i.e., phonon transport.

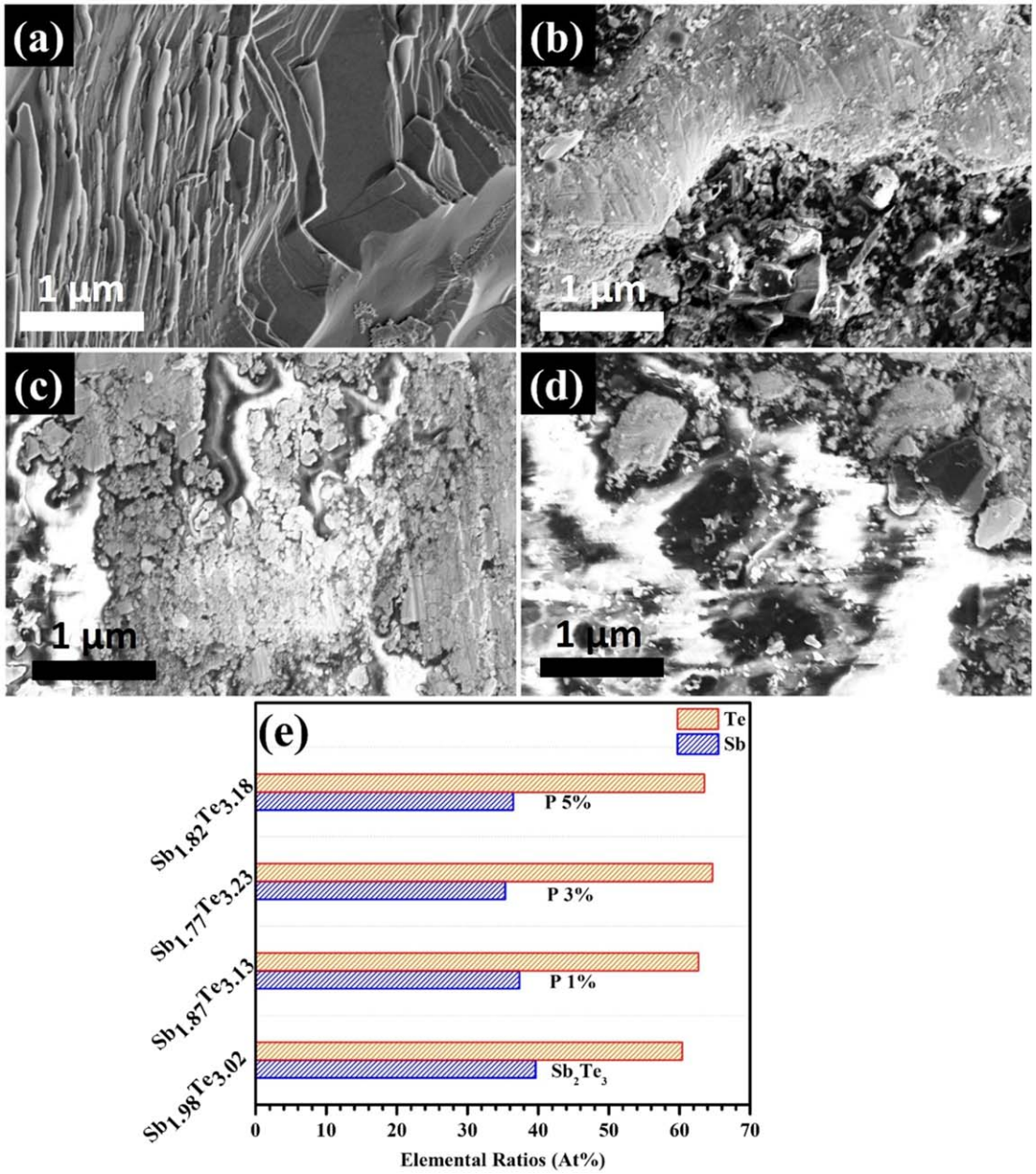

Figure 3. (a)–(e) SEM images of $PMMA_xSb_2Te_3$/5%Te (x = 0.00, 0.01, 0.03, 0.05) nanocomposite prepared by melt-quenching process (a) 0.00, (b) 0.01, (c) 0.03, (d) 0.05, (e) EDX composition ratio.

The XPS of Sb 3d and Te 3d are displayed in figures 5(f) and (g), respectively. Using the Gaussian-Lorentzian (GL) function, the XPSPEAK41 program deconvoluted the generated XPS peaks. Sb 3d has three peaks at ~530 eV, ~532 eV, and ~539 eV, which correspond to the ground state (3d5/2), O 1 s state, and excited state (3d3/2), respectively, while Te 3d exhibits two peaks at ~576 eV and ~586 eV, which correspond to the ground state (3d5/2), and the excited state (3d3/2), respectively. The oxidation states of Sb is 3+ and that of Te is 2- are confirmed by the energy gap between the excited state and ground state (E = 3d3/2–3d5/2 = ~9.3 eV for Sb and ~10.4 eV for Te, respectively) [44]. This XPS results again confirm the phase formation of the Sb_2Te_3/Te composite.

3.4. Thermoelectric transport properties

The electrical transport properties of polymer mixed Sb_2Te_3/Te nanocomposites measured in the temperature range 300–400 K were presented in figure 6.

Figure 6(a) shows the temperature-dependent electrical conductivity of polymer-mixed Sb_2Te_3/Te nanocomposites. All the samples show metallic behavior with a decrease in electrical conductivity with increasing temperature. This might be caused by the interaction of the scattering mechanisms known as grain boundary/interfacial (metal-semiconductor) potential barrier scattering and acoustic phonon scattering (APS).

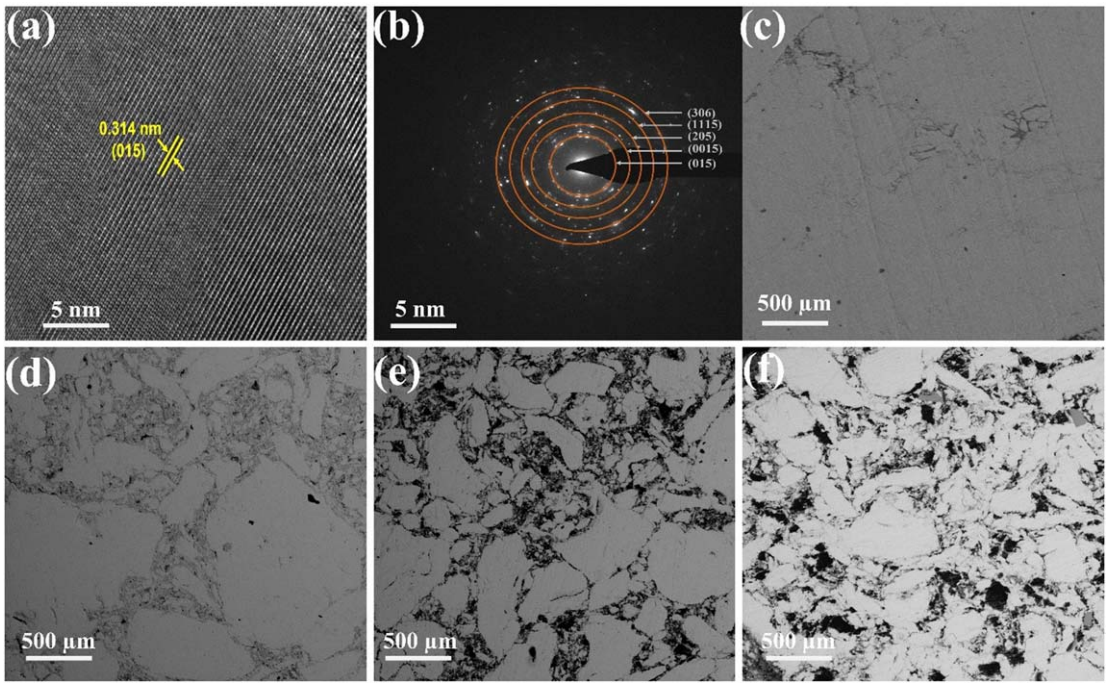

Figure 4. (a) HR-TEM image (b) SAED pattern and (c-f) BSE images of $PMMA_xSb_2Te_3/5\%Te$ (x = 0.00, 0.01, 0.03, 0.05) nanocomposite prepared by the melt-quenching process.

[39–42]. The pristine Sb_2Te_3 sample shows a higher electrical conductivity value of 70×10^3 S m^{-1} compared to other polymer mixed samples. The electrical conductivity value displays a decreasing trend with increasing the polymer content from 1% to 5%. From figure 6(a), the polymer mixed samples show a lower electrical conductivity due to hindrance in the transport of electrons between the metal and polymer interface. At a specific temperature, the observed fluctuation in the electrical conductivity value is directly related to the variation in carrier concentration (n_c) and carrier mobility (μ) and is represented as $\sigma = n_c e\mu$ [41, 42]. The Hall measurements were performed for all the samples at room temperature and the measured Hall mobility and carrier concentration values were presented in table 1. The carrier mobility shows a decreasing trend from the value of 67.21 cm^2/V.s to 5.43, 0.18, and 0.065 cm^2/V.s for 1% polymer, 3% polymer, and 5% polymer nanocomposites respectively. Pristine Sb_2Te_3/Te and polymer mixed nanocomposite show carrier concentration values in the range of 10^{20} cm^{-3}. The decrease in both carrier concentration and carrier mobility values of polymer mixed nanocomposites resulted in low electrical conductivity values.

Figure 6(b) shows the temperature-dependent Seebeck coefficient values for the pristine and polymer-mixed nanocomposites. The pristine sample shows p-type conductivity whereas the polymer mixed Sb_2Te_3/Te nanocomposites show n-type conductivity. As mentioned in table 1, the 'Te' phase is increased from 8% to 18% and the atomic percentage of 'Te' increased from 60.4 at% to 63.6 at%. This increase in 'Te' segregation can be directly correlated with the carrier concentration (table I) and Seebeck coefficient measurements (figure 6(b)). It is clearly evident, that the carrier type has been changed from 'p-type' to 'n-type' in Seebeck coefficient measurement as well as the electron concentration increases from 0.89×10^{20} to 25.19×10^{20} with increasing PMMA content. In the case of increased 'Te' content in the Sb_2Te_3/Te polymer composites, the reduction in hole density of the composite might be due to the following reasons (i) The density of states (DOS) of 'Te' is smaller than the DOS of Sb_2Te_3 and hence in the condition of increasing 'Te' contribution, the overall DOS and the releasing of holes to the polymer composites can be reduced. (ii) In the case of Sb vacancy, Sb atoms from Te sites will return back to Sb sites, and Te vacancy will become dominant and contributes excess electrons. Hence, we can conclude that with increasing PMMA, the 'Te' gets more segregation and the associated defects such as antisite defects, and vacancies may enhance the concentration of electrons and reverse the conductivity from p to n-type [26, 45]. All the samples follow a similar trend, i.e., the magnitude of the S values increases with temperature, indicating a metallic behavior. This temperature-dependent trend is consistent with the reduction of σ with an increase in temperature. The linear temperature dependency of S may mean that the dominant mechanism of carrier transportation under a temperature gradient is diffusive in nature [42, 46]. The enhancement in the Seebeck coefficient with temperature in polymer mixed Sb2Te3 composites may be attributed to the filtering of low energy charge carriers by the addition of PMMA embedded inside the Sb_2Te_3 grain boundaries. The transition from p-type to n-type in the polymer matrix with the increase of PMMA might

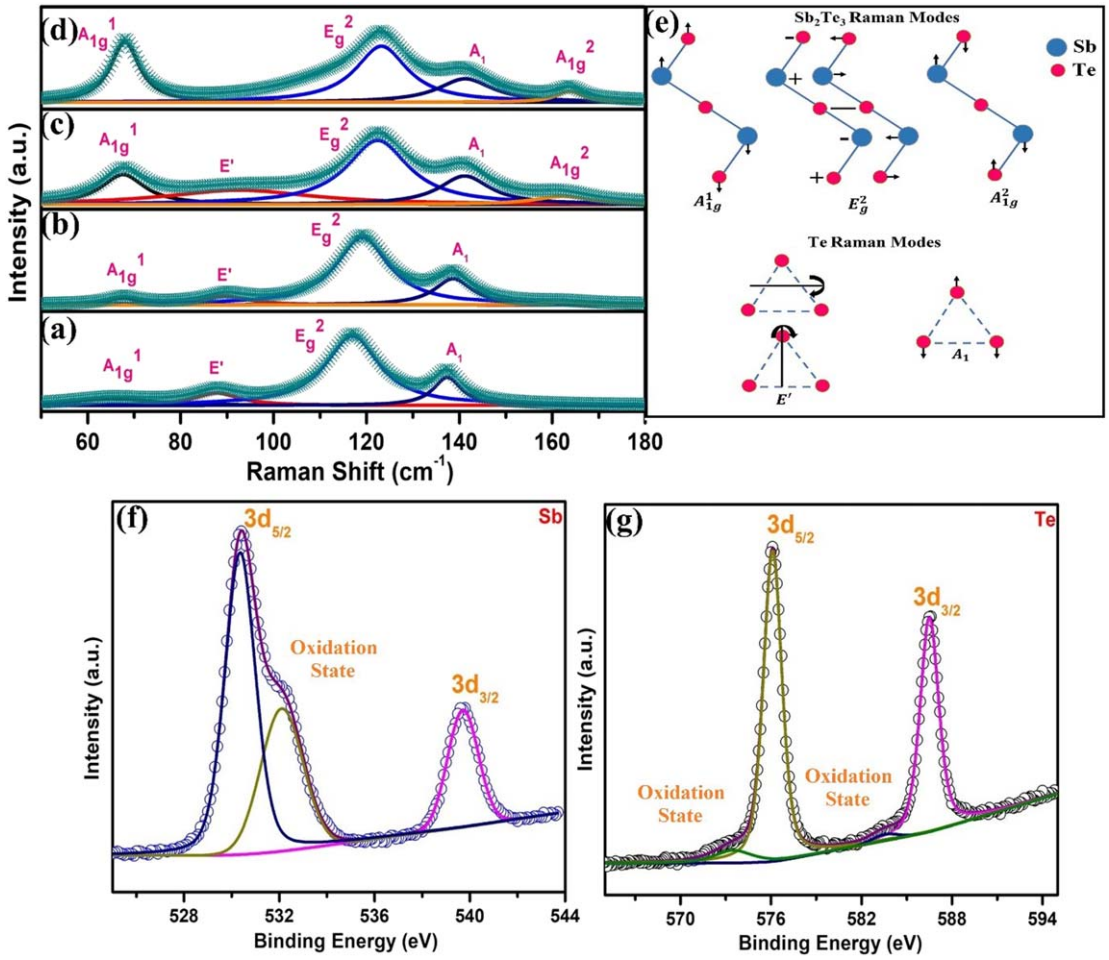

Figure 5. (a)–(d) Raman spectra images of polymer mixed Sb_2Te_3/Te nanocomposite with $PMMA_x$-Sb_2Te_3/Te (x = 0.00, 0.01, 0.03, 0.05) weight % ratio of total Sb_2Te_3/Te, (e) Raman active modes of Sb_2Te_3 and Te, (f) XPS of Sb, and, (g) XPS image of Te of polymer mixed Sb_2Te_3/Te nanocomposite prepared by the melt-quenching process.

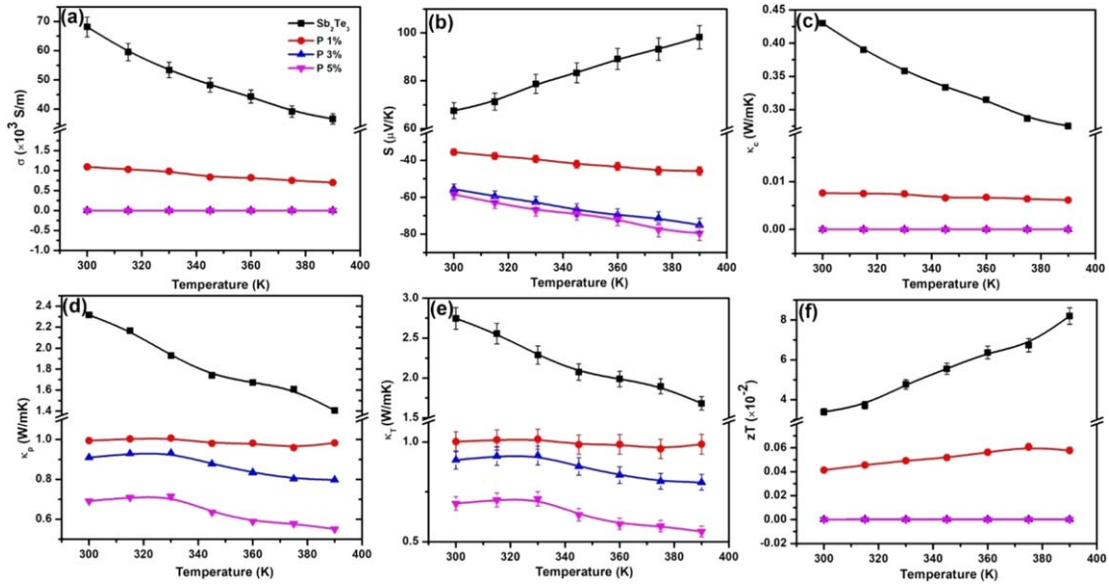

Figure 6. $PMMA_x$-Sb_2Te_3/Te (x = 0.00, 0.01, 0.03, 0.05), temperature-dependent of (a) Electrical conductivity, (b) Seebeck coefficient, (c) electronic part of thermal conductivity, (d) Lattic part of thermal conductivity (e) Total thermal conductivity, and (f) zT.

be the cause of an increase in segregated Te phases which is clearly evident in XRD analysis. The observed results including carrier concentration, carrier mobility, and Seebeck coefficient supports the transition from p-type to n-type.

Figure 6(e) shows how thermal conductivity varies with temperature (κ_c). In the case of narrow bandgap materials, i.e., Sb_2Te_3 and Bi_2Te_3, the total thermal conductivity is the sum of carrier (κ_c), phonon (κ_p), and bipolar thermal conductivity (κ_b), i.e., it can be expressed as $\kappa_T = \kappa_c + \kappa_p + \kappa_b$ [39–41, 44]. At low temperature, below 423 K, κ_b is negligible. The κ_c value is estimated from Wiedemann–Franz relation $\kappa_c = L\sigma T$, L is the Lorenz number in this case. [39–41, 44]. The single parabola band (SPB)-APS approximation is used to determine the L values from the S values. [40–42, 45–47]. The κ_c shows a similar trend of electrical conductivity, the decrease in carrier thermal conductivity with increasing temperature. Another reason for decreasing the electrical part of thermal conductivity is the density of the material. The decrease in density of Sb_2Te_3 upon the addition of polymer affects the carrier transport. From figure 6, it can be seen that κ_c contributes around ~15%, whereas κ_p dominates the κ value, contributing around ~85% of total κ. In general, the κ drops with rising temperature as a result of phonon-phonon scattering, phonon-carrier scattering, and phonon interface scattering at Te nanograins [41, 42]. The temperature-dependent phonon thermal conductivity (κ_p) and total thermal conductivity (κ_T) plots are depicted in figures 6(d) and (e) respectively. Both the plots show a decreasing trend with increasing temperature. The total thermal conductivity of the pristine Sb_2Te_3/Te sample shows a value of 2.75 W m^{-1} K^{-1}. However, with the increase of polymer content in Sb_2Te_3/Te, the thermal conductivity values are found to decrease up to 0.4 W/m/K for 5% polymer.

It should be mentioned that though the polymer addition brings interesting changes like reduction in thermal conductivity and conduction reversal from p to n-type, the figure of merit is found to decrease as shown in figure 6(f). In the present study, the higher zT value of 8×10^{-2} was obtained for the pristine sample, and it almost decreased nearly to zero for the polymer added samples. In summary, the addition of polymer with Sb_2Te_3/Te nanocomposites resulted in a decrease in density, electrical conductivity, conduction reversal from p to n-type, and a reduction in thermal conductivity values.

4. Conclusions

The thermoelectric properties of poly methyl methacrylate (PMMA) polymer mixed Sb_2Te_3/Te nanocomposites made by melt-quenching followed by ball milling processes have been studied. The addition of polymer has a considerable impact on Sb_2Te_3/Te nanocomposites thermoelectric characteristics studied in the temperature range 300 to 390 K. A 30% reduction in thermal conductivity with the 5% PMMA composites has been observed. On the other hand, the polymer addition has significantly decreased the electrical conductivity. The addition of polymer also changes the conduction type from p to n-type. The positive impact of polymer addition in reducing thermal conductivity may help in designing high-performance thermoelectric materials based on Sb_2Te_3 composites.

Acknowledgments

Authors thank CSIR India is acknowledged for funding through Grant No: SP/CSIR-19-0004.

Data availability statement

All data that support the findings of this study are included within the article (and any supplementary files).

Credit authorship contribution statement

Dilip Kumar Meena: Conceptualization, Writing-original draft, Supported to the experimental work, Data curation, Writing-review & editing. Rapaka S C Bose: Conceptualization, Data curation, Supervision, Writing-original draft, review & editing. A M Umarji: Conceptualization, Supported to the experimental work. D Arvindha Babu: Conceptualization, Supported to the experimental work.

Declaration of competing interest

The authors declare that they have no known competing financial interests or personal relationships that could have appeared to influence the work reported in this paper.

ORCID iDs

Dilip Kumar Meena https://orcid.org/0000-0001-6512-0052
A M Umarji https://orcid.org/0000-0002-3167-7060

References

[1] Tritt T M and Subramanian M A 2006 Thermoelectric materials, phenomena, and applications: a bird's eye view *MRS Bull.* **31** 188–98
[2] Kim H S, Liu W and Ren Z 2017 The bridge between the materials and devices of thermoelectric power generators *Energy Environ. Sci.* **10** 69–85
[3] Bubnova O 2012 Towards polymer-based organic thermoelectric generators *Energy Environ. Sci.* **5** 9345
[4] Azghandi S H M, Ahmadabadi V G, Raoofian I, Fazeli F, Zare M, Zabett A and Reihani H 2015 Invesigation on decomposition behaviour of austenite under continous colling in vanadium microalloyed steel (30MSV6) *Mater. Des.* **88** 751–8
[5] Bala M, Masarrat A, Kumar V, Ojha S, Asokan K and Annapoorni S 2020 Effect of thermal annealing on thermoelectric properties of $Bi_xSb_{2-x}Te_3$ *thin films grown by sputtering, J. Appl. Phys.* **127** 245108–01–12
[6] Kajikawa T, Serizawa M and Kamio K 2002 Annealing effect on thermoelectric performance for hot-press sintered chromium disilicide ($CrSi_2$) *Int. Conf. Thermoelectr. ICT, Proc.* **2002** 94–7
[7] Bose R S C, Rangaraj L and Nag A 2017 Process dependent thermoelectric transport properties of $Ca_3Co_4O_9$ *Adv. Mater. Proc.* **2** 485–91
[8] Madavali B, Kim H S, Choi M G, Park G C, Koo J M, Son H T and Hong S J 2016 Effect of sintering temperature on thermoelectric properties of p-Bi_2Te_3 alloys produced by gas atomization *Int. J. Appl. Ceram. Technol.* **13** 245–51
[9] Yonggao Y, Xinfeng T, Haijun L, Lingling Y and Qingjie Z 2007 Cooling rate dependence of microstructure and thermoelectric properties of $AgPb_{18}SbTe_{20}$ compounds *Int. Conf. Thermoelectr. ICT, Proc.* **119** 1–3
[10] Wang S Y, Xie W J, Li H, Tang X F and Zhang Q J 2011 Effects of cooling rate on thermoelectric properties of n-type $Bi_2(Se_{0.4}Te_{0.6})_3$ compounds *J. Electron. Mater.* **40** 1150–7
[11] Bose R S C and Nag A 2017 Methodology oriented thermoelectric transport properties of $CaMn_{0.98}Nb_{0.02}O_3$ *International Journal of Scientific & Engineering Research* **8** 1189–93
[12] Paul S, Pal U and Pradhan S K 2021 Grain size mediated electrical and thermoelectric performances of mechanically alloyed Sb2Te3 nanoparticles *J. Alloys Compd.* **858** 157732
[13] Trung T Q and Lee N E 2016 Flexible and stretchable physical sensor integrated platforms for wearable human-activity monitoringand personal healthcare *Adv. Mater.* **28** 4338–72
[14] Lee J W, Xu R, Lee S, Jang K I, Yang Y, Banks A and Rogers J A 2016 Soft, thin skin-mounted power management systems and their use in wireless thermography *Proc. Natl Acad. Sci.* **113** 6131–6
[15] Shi D, Wang R, Wang G, Li C, Shen X and Nie Q 2017 Enhanced thermoelectric properties in Cu-doped Sb_2Te_3 films *Vacuum* **145** 347–50
[16] Kumar K D A, Meena D K, Bose R S C, Meena R, Murahari P, Mele P and Ramesh K 2021 Optical and thermoelectric properties of Sb_2Te_3/ZnTe nanostructured composites *J. Alloys Compd.* **865** 158621
[17] Kim J, Zhang M, Bosze W, Park S D, Lim J H and Myung N V 2015 Maximizing thermoelectric properties by nanoinclusion of γ-SbTe in Sb_2Te_3 film via solid-state phase transition from amorphous Sb-Te electrodeposits *Nano Energy.* **13** 727–34
[18] Cao Y Q, Zhao X B, Zhu T J, Zhang X B and Tu J P 2008 Syntheses and thermoelectric properties of Bi_2Te_3/Sb_2Te_3 bulk nanocomposites with laminated nanostructure *Appl. Phys. Lett.* **92** 90–3
[19] Das S *et al* 2021 Sb_2Te_3/graphite nanocomposite: a comprehensive study of thermal conductivity *J. Materiomics* **7** 545–55
[20] Kumar S, Faraz M and Khare N 2019 Enhanced thermoelectric properties of Sb_2Te_3 - graphene nanocomposite *Mater. Res. Express* **6** 085079
[21] Lee M H, Kim K R, Rhyee J S, Park S D and Snyder G J 2015 High thermoelectric figure-of-merit in Sb_2Te_3/Ag_2Te bulk composites as Pb-free p-type thermoelectric materials *J. Mater. Chem.* C **3** 10494–9
[22] Ghosh, Ahmad M, Bisht P and Mehta B R 2021 Modifying the thermoelectric transport of Sb_2Te_3 thin films via the carrier filtering effect by incorporating size-selected gold nanoparticles *ACS Appl. Mater. Interfaces* **13** 13226–34
[23] Kul'bachinskii V A 2019 Nanostructuring and creation of nanocomposites as a promising way to increase thermoelectric efficiency *Nanotechnologies Russ.* **14** 334–45
[24] Shen S, Zhu W, Deng Y, Zhao H, Peng Y and Wang C 2017 Enhancing thermoelectric properties of Sb_2Te_3 flexible thin film through microstructure control and crystal preferential orientation engineering *Appl. Surf. Sci.* **414** 197–204
[25] Chen J *et al* 2010 Sb_2Te_3 nanoparticles with enhanced seebeck coefficient and low thermal conductivity *Chem. Mater.* **22** 3086–92
[26] Wu Z, Chen X, Mu E, Liu Y, Che Z, Dun C, Sun F, Wang X, Zhang Y and Hu Z 2020 Lattice strain enhances thermoelectric properties in Sb_2Te_3/Te heterostructure *Adv. Electron. Mater.* **6** 1–9
[27] Ceyda Yelgel Ö and Srivastava G P 2013 Thermoelectric properties of p-type $(Bi_2Te_3)_x(Sb_2Te_3)_{1-x}$ single crystals doped with 3wt% Te *J. Appl. Phys.* **113** 733709–1–8
[28] Il Kim S *et al* 2015 Dense dislocation arrays embedded in grain boundaries for high-performance bulk thermoelectrics *Science* **348** 109–14
[29] Kim S, Ryu S H, Kwon Y T, Lim H R, Park K R, Song Y and Choa Y H 2017 Synthesis and thermoelectric characterization of high-density Ag_2Te nanowire/PMMA nanocomposites *Mater. Chem. Phys.* **190** 187e193
[30] Akram R, Khan J S, Qamar Z, Rafique S, Hussain M and Kayani F B 2022 Ultra-low thermal conductivity and thermoelectric properties of polymer-mixed Bi2Te3 nanofibers by electrospinning *J. Mater. Sci.* **57** 3309–21
[31] Lee H J *et al* 2016 Enhanced thermoelectric performance of PEDOT: PSS/PANI–CSA polymer multilayer structures *Energy Environ. Sci.* **9** 2806–11
[32] Goo G, Anoop G, Unithrattil S, Kim W S, Lee H J, Kim H B, Jung M H, Park J, Ko H C and Jo J Y 2019 Proton-irradiation effects on the thermoelectric properties of flexible Bi_2Te_3/PEDOT:PSS composite films *Adv. Electron. Mater.* **5** 1800786
[33] Kim W S *et al* 2020 Feasible tuning of barrier energy in PEDOT:PSS/Bi_2Te_3 nanowires-based thermoelectric nanocomposite thin films through polar solvent vapor annealing *Nano Energy* **67** 104207
[34] Khan J S, Akram R, Husaain M, Rafique S, Kayani F B and Rehman A 2023 Feasible tuning of barrier energy in PEDOT:PSS/Bi_2Te_3 nanowires-based thermoelectric nanocomposite thin films through polar solvent vapor annealing *Polym. Compos.* **67** 1–12

[35] Wang Y Y, Cai K F and Yao X 2012 One-pot fabrication and enhanced thermoelectric properties of poly(3,4-ethylenedioxythiophene)-Bi_2S_3 nanocomposites *J. Nanopart. Res.* **14** 848
[36] Dubey N and Leclerc M 2011 Conducting polymers: efficient thermoelectric materials *J. Polym. Sci. B: Polym. Phys.* **49** 467–75
[37] Tian Z H, Liu H H, Wang N, Liu Y X and Zhang X X 2018 Facile preparation and thermoelectric properties of PEDOT nanowires/Bi_2Te_3 nanocomposites *J. Mater. Sci., Mater. Electron.* **29** 17367–73
[38] Thonhauser T, Jeon G S, Mahan G D and Sofo J O 2003 Stress-induced defects in Sb_2Te_3 *Phys. Rev. B - Condens. Matter Mater. Phys.* **68** 1–6
[39] Bose R S C, Dilip K M, Mele P and Ramesh K 2021 Role of grain alignment and oxide impurity in thermoelectric properties of textured n-type Bi–Te–Se alloy *J. Phys. D: Appl. Phys.* **54** 235503
[40] Meena D K, Bose R S C and Ramesh K 2022 Melt solidification rate-dependent structural and thermoelectric properties of Sb_2Te_3/Te nanocomposites *J. Alloys Compd.* **902** 163767
[41] Meena D K, Bose R S C, Vinoth S and Ramesh K 2022 Impact of melt solidification rate on structural and thermoelectric properties of n-type Bi_2Te_3 alloy *Appl. Phys.* **128** 528
[42] Malik K, Das D, Neogi S K, Deb A K, Dasgupta A, Bandyopadhyay S and Banerjee A 2016 The effect of quenching from different temperatures on $Bi_{0.88}Sb_{0.12}$ alloy *J. Phys. Chem. Solids* **91** 7–128
[43] Xie W *et al* 2010 Identifying the specific nanostructures responsible for the high thermoelectric performance of $(Bi,Sb)_2Te_3$ nanocomposites *Nano Lett.* **10** 3283–9
[44] Bose R S C, Sheoran V, Vaishnavi P S H, Prem D S, Chakravarty S, Raman R, Babu D A, Saharan P, Nair S and Ram J 2020 Anisotropic thermoelectric transport in textured $Sb_{1.5}Bi_{0.5}Te_3$ nanomaterial synthesized by facile bottom-up physical process *J. Alloys Compd.* **859** 157828
[45] Wei M *et al* 2022 Directional thermal diffusion realizing inorganic Sb_2Te_3/Te hybrid thin films with high thermoelectric performance and flexibility *Adv. Funct. Mater.* **32** 2207903
[46] Wang J *et al* 2021 Enhancing thermoelectric performance of Sb_2Te_3 through swapped bilayer defects *Nano Energy* **79** 105484
[47] Ojo O P, Thompson A and Nolas G S 2021 *Mater. Sci. Semicond. Process.* **133** 10597922